THE CHARGE COMPOSITION AND ENERGY SPECTRA OF COSMIC-RAY NUCLEI FROM 3000 MeV PER NUCLEON TO 50 GeV PER NUCLEON

J. A. LEZNIAK AND W. R. WEBBER

Physics Department, University of New Hampshire, Durham

ABSTRACT

We present new data on the energy spectrum and charge composition of cosmic-ray nuclei with $3 \leq Z \leq 28$. These data were obtained using a large-area multielement balloon-borne telescope containing scintillation counters, UVT Lucite Cerenkov detectors, and a Freon gas Cerenkov detector. The energy spectra and charge ratios have been measured over the energy range from ~ 300 MeV per nucleon to ~ 50 GeV per nucleon. We find that the data above ~ 1 GeV per nucleon is consistent with a cosmic-ray escape length $X(E) = (7.2 \pm 1.2)E^{-0.30 \pm 0.06}$ g cm^{-2}, where E is the kinetic energy in units of GeV per nucleon. This energy dependence can be reconciled with a Kolmogorov spectrum of interstellar scattering irregularities in a simple resonant scattering model for cosmic-ray diffusion in the Galaxy. The changes in primary-to-primary nucleus ratio we observe, including those involving Fe nuclei, are consistent with this escape-length variation and do not require the assumption of different source spectra for different nuclei. We note that because of this escape-length variation with energy, the exponent μ of the source spectrum of cosmic rays $[q(E) \sim E^{-\mu}]$ must be 0.3 smaller than that of the higher energy spectra observed at Earth. In analogy to the helium spectrum, it is concluded that the exponents of the source spectra of heavier cosmic-ray nuclei are probably not constant with energy but increase slowly from ~ 1.95 at an energy ~ 5 GeV per nucleon to 2.45 above 100 GeV per nucleon. Utilizing the individual charge ratios measured over a broad range of energies, we have determined a new set of cosmic-ray source abundances. The relative abundances of N, Na, Si, Ca and Fe differ from some earlier determinations. The behavior of the charge ratios below 1 GeV per nucleon is examined, and it is concluded that the evidence is contradictory regarding the continuation of an energy-dependent path length at lower energies.

Subject headings: cosmic rays: abundances — cosmic rays: general

I. INTRODUCTION

Recently it has been possible to measure the charge composition of primary cosmic rays with increasing precision. Extrapolation of these measurements back to the cosmic-ray source, using a model for galactic propagation, has then allowed the source composition of these particles to be deduced (e.g., Shapiro and Silberberg 1975). At the same time our understanding of the energy spectra of these nuclei has increased greatly, and with more refined measurements it has been observed that the energy spectra of the various nuclear species are different (Juliusson, Meyer, and Müller 1972; Webber *et al.* 1973; Ormes and Balasubrahmanyan 1973; Smith *et al.* 1973). As a result of this the charge composition of the cosmic radiation is energy dependent, and the determination of the source composition becomes a more complicated procedure. The causes for these energy-dependent effects must be determined before one can claim to understand the problem of source composition and propagation of cosmic rays. To achieve this goal requires high-precision abundance data over several decades in energy, preferably obtained by the same instrument. To date, individual measurements

have not extended over about one decade in energy, and to get an overall picture of the problem of energy spectrum and charge composition it has been necessary to piece together measurements of different observers using different experimental techniques (e.g., Lund 1975).

At the same time the methods used to derive the cosmic-ray energy spectrum itself have become more sophisticated. Early spectral determinations using solid and gas Cerenkov detectors (Webber, Damle, and Kish 1972; Juliusson 1974) used a very simple procedure for unfolding the energy spectrum from the Cerenkov pulse height distribution. High-energy spectral measurements were also made using magnetic spectrometers (Smith *et al.* 1973) and total energy calorimeters (Balasubrahmanyan and Ormes 1973). New observations of the energy spectra of cosmic-ray nuclei at high energies have been reported using a combination of two gas Cerenkov counters (Caldwell 1977).

Recently Lezniak (1975) has developed a rigorous mathematical technique for deriving energy spectra from the measured pulse-height distributions in solid or gas Cerenkov counters. This work has been extended to include the effects of knock-on electrons

676

(Lezniak 1976), which are important from the point of view of correctly unfolding the spectrum from this type of counter. In this paper we present results on the charge composition and energy spectra for nuclei with $Z = 2$–28, obtained on three balloon flights in 1974 and one flight in 1976. These measurements have been made using a large-area telescope containing several detector elements including a solid and a gas Cerenkov detector to span in a nearly continuous fashion two decades of energy from ~ 300 MeV per nucleon to $\geqslant 50$ GeV per nucleon.

II. INSTRUMENTATION

The instrument used in these studies is an enlarged and improved version of the multielement telescope used in this laboratory for previous studies of the cosmic-ray charge and isotope composition (Webber, Damle, and Kish 1972; Webber, Lezniak, and Kish 1973). An outline drawing of the 1974 and 1976 versions of the charge and energy spectrum part of this telescope is given in Figure 1. The telescope itself is a multipurpose instrument designed to measure the isotopic composition of cosmic rays using both the $dE/dx \times E$ and $C \times E$ techniques, in addition to the charge and energy spectral measurements. The upper section of this telescope, consisting of two scintillation counters and both a Lucite and a gas Cerenkov counter, is used for the charge and energy spectral measurements reported here. This part of the telescope is basically the same in 1974 and 1976 except for the addition of a second UVT Lucite Cerenkov counter in the later version. A telescope "event" is determined by a coincidence between scintillators S1 and S2; the resulting geometry factor is 824 cm² sr. (In 1976 a wide-angle mode consisting of a coincidence between S1 and C2 was also employed for the analysis of gas Cerenkov detector events. This mode had a geometrical factor of 1470 sr cm².) Each of the counters in this mode is viewed by several photomultiplier tubes as indicated in the figure—in a white diffusion box configuration. The uniformity of light output as a function of position in all counters is a very important quantity related to the resolution re-

quired to separate adjacent charges and to derive an accurate energy spectrum. Each detector is first compensated using a white mask technique (Webber, Damle, and Kish 1972; Webber, Lezniak, and Kish 1973), so that the mean pulse height for a collimated-monoenergetic MeV electron source is uniform to better than 2% FWHM for a large number of points taken at random over the surface of each detector.

The individual detecting elements are curved to reduce path-length effects from particles coming in at different zenith angles. When this procedure is used, the maximum path-length difference in the worst counter (the Lucite Cerenkov counter) is $\sim 12\%$. This is still not sufficient to achieve individual charge resolution throughout the range up to $Z = 26$. To further reduce the path-length variations, a "radial" measurement is made in a thin scintillator S1' located directly below S1. The radial counter is characterized by a rapid falloff in pulse height with radius as well as azimuthal symmetry. Assuming the particle does not interact in S1 or S1', a normalized ratio S1'/S1 provides a measure of the radius in S1 to within ± 3 cm FWHM. Once this radius is known, an average correction to the path length in C2 and S2 is made. The details of this procedure are discussed by Simpson (1977). Basically the residual path-length variations are reduced to less than 4% FWHM after this correction is made. This is now less than the intrinsic resolution for all detectors over essentially the entire charge range. The intrinsic resolution for both scintillation and Cerenkov detectors of similar thickness to those used in this experiment is discussed in detail in several papers (e.g., Webber, Lezniak, and Kish 1973).

An understanding of the basic properties of the Lucite and gas Cerenkov detectors is essential for understanding the data to be presented later; therefore we briefly discuss these counters at this time. For the UVT Lucite counter we have determined an effective index of refraction which is equal to 1.51—corresponding to a Cerenkov threshold of 312 MeV per nucleon. This piece of Lucite, 2 cm thick, is viewed by twelve 5 inch photomultiplier tubes giving a value of $\sim 18\%$ for the ratio of phototube to total internal surface area. The total light collection efficiency of this
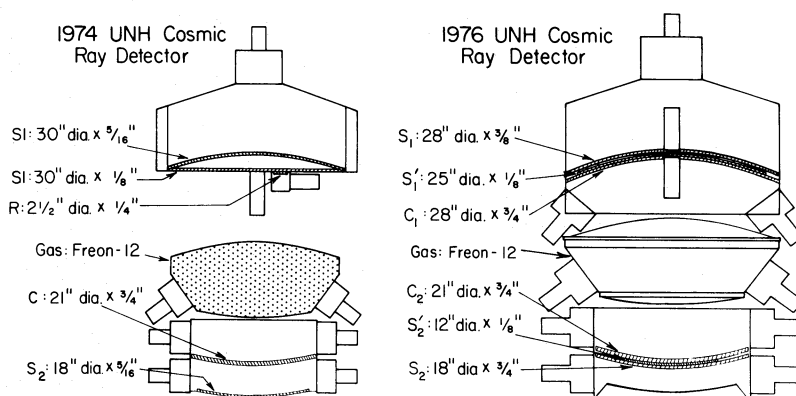

FIG. 1.—Outline drawing of charge and energy measurement modules of 1974 and 1976 telescopes

counter is ~40%, and the FWHM distribution for $Z = 1$, $\beta = 1$ particles is measured to be 48%—corresponding to ~42 photoelectrons produced at the photocathodes of the 12 photomultiplier tubes. This resolution should scale as

$$[Z(1 - \beta_0^2/\beta^2)^{1/2}]^{-1} , \qquad (1)$$

where Z = the charge, and β_0 = threshold velocity of the Cerenkov counter, subject to the experimental limitations noted above.

The gas Cerenkov detector is composed of a 25 cm thick chamber of Freon-12 gas. In 1974 this detector was operated at a gauge pressure of 29.5 pounds per square inch (2 atm) at 22.5° C. This gives an index of refraction = 1.00338 corresponding to a Cerenkov threshold of 10.5 GeV per nucleon. In 1976 the gauge pressure was 40.2 pounds per square inch, giving an index of refraction = 1.00451 corresponding to a Cerenkov threshold of 9.0 GeV per nucleon. The photons produced by a traversing relativistic cosmic ray are diffusively reflected in this counter and collected by two separate banks of four 5 inch (12.7 cm) photomultiplier tubes. The light collection efficiency for this arrangement is ~40%; and the FWHM distribution for $Z = 1$, $\beta = 1$ particles is ~100% at a pressure of 40 pounds per square inch corresponding to ~7 photoelectrons produced at the photocathode. This resolution scales in the same way with charge and energy as the UVT Lucite counter.

The Lucite counter has a small residual scintillation which amounts to ~4% of the signal for $\beta = 1$ particles. In the case of the gas Cerenkov detector the dominant "nondirect Cerenkov contribution" to the total signal is neither residual scintillation nor knock-on electron Cerenkov light produced within the detector itself but rather Cerenkov light generated within the Lucite windows of this detector by knock-on electrons. This component has been studied by examining the below-threshold response of the gas Cerenkov detector. It is proportional to Z^2 and contributes 10% of the $\beta = 1$ signal at the Cerenkov threshold. The resolution of this component appears

to have the same variation with pulse height as the "direct Cerenkov light."

III. BALLOON FLIGHTS

The instrument illustrated in Figure 1 was flown three times on high-altitude balloons in the summer and fall of 1974 and again in the fall of 1976. The pertinent details of the balloon flights are shown in Table 1.

Spectral data from the UVT Lucite Cerenkov detector come from the first two high-latitude flights. Data from the Freon gas Cerenkov detector come from the later two flights at Sioux Falls. The total weight of the scientific payload was ~500 Kg. The data was telemetered to a ground station via a 20 kHz subcarrier. Each data word was ~160 bits long and contained 12 × 12 bit words (corresponding to 4096 channel analysis for each of the detectors) plus housekeeping and parity bits.

IV. THE RAW DATA

The videotape recordings made during the balloon flights are first reformatted into computer tapes. Various combinations of two-dimensional matrices were then constructed for pairs of counters on an hourly basis for the float data of each flight. The hourly data were used to correct for small gain changes during a flight because of temperature changes in the gondola. This was accomplished by identifying the pulse height of the $\beta = 1$ peak for several prominent nuclei such as He, C, O, Mg, S, and Fe in each detector. These gain corrections were ≤5% in all cases. All data were renormalized for these gain changes and for path-length corrections, and a master tape for each flight was produced. Separate tapes were then made from this master tape covering various classes of events. These tapes were used to construct the multidimensional matrices used for data analysis. For the charge and energy analysis in this paper we will be using the following counters: the S1 and S2 scintillators, the UVT Lucite Cerenkov counters C1 and C2, and the Freon gas Cerenkov counter G, which is the sum of two separate banks G1 and G2.

TABLE 1

BALLOON FLIGHT DETAILS

Date	Location	Cutoff (GV)	Avg. Altitude (g cm⁻²)	Collection Factor (m² sr⁻¹ s⁻¹)	Mt. Washington Neutron Monitor
1974 July 21	Churchill	≲0.2	2.9	4,120	2149
1974 Aug. 3	Churchill	≲0.2	2.1	2,880	2247
1974 Sept. 22	Sioux Falls	~1.4	3.0	7,640	2178
1976 Sept. 24	Sioux Falls	~1.4	3.8	8,440	2392

V. DATA ANALYSIS PROCEDURES

a) Application of Consistency Requirements

Before energy spectra of individual elements can be unfolded from the pulse height distributions, it is necessary to have sufficiently good charge resolution that contamination of even the most rare chemical species by more abundant neighboring elements is negligible. This requires a high level of intrinsic charge resolution as well as good background rejection. Background rejection for particles interacting in the telescope may be accomplished by applying consistency requirements on the pulse heights of the various telescope elements. These criteria, if applied carefully, will not remove a significant fraction of the noninteracting particles and will provide a more effective way of removing background events than the use of guard counters. Because several types of consistency requirements can be applied and compared for a single data set, this approach is much less susceptible to charge-dependent corrections that are present when guard counters are used. We have considered a variety of consistency criteria, for the analysis of the data utilizing all five counters, and have varied these criteria in a systematic way to study the effects on the removal of background and on the removal of so-called good events due to noninteracting particles with trajectories within the telescope geometry. We find that a simple criterion involving
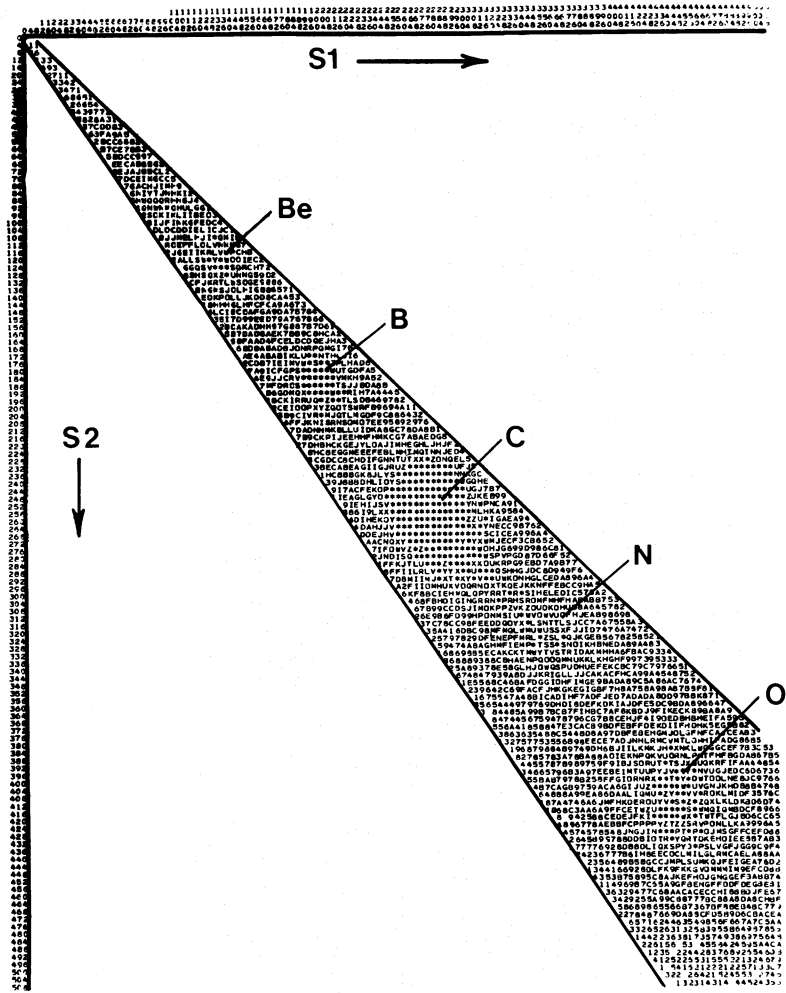

FIG. 2.—Matrix of events showing pulse heights in S1 and S2 scintillators. The selection criterion accepts only those events that lie between the two lines.

only the S1 and S2 counters is generally as effective for removing background events as more elaborate criteria involving several counters. It is also easier to interpret and we believe it to be more free of possible systematic charge-dependent effects introduced when several parameters are compared. To illustrate how this selection criterion operates, we show in Figure 2 a matrix of events showing the pulse height in scintillator S1 versus the pulse height in S2. The pulse heights of noninteracting nuclei will be correlated in these two counters since they are normalized to have equal gain. We then apply a selection criterion of the form

$$\frac{2|S1 - S2|}{S1 + S2} < X\rho, \qquad (2)$$

where ρ is a function which is proportional to the

fractional resolution of the (S1 + S2) signal at low signal levels and is equal to 1 at high signal levels; and X is a parameter. The width of the selection band is changed by varying X between 0.2 and 0.5 to study the effects on both the background and good events on the matrices under study. For charge composition studies using the solid Čerenkov detectors where $E > 312$ MeV per nucleon, optimum rejection of background is achieved with $X = 0.3$. This corresponds to a selection passband $\gtrsim 3\,\sigma$ for all charges, where σ is the observed resolution at a given (S1 + S2) pulse height as determined from the individual charge distributions. This criterion is found to eliminate less than 2% of the noninteracting nuclei, and this small fraction is verified to be essentially charge and energy independent. The number of background events, caused mainly by interacting nuclei, is reduced by 80–90% on the final matrices by this criterion. An
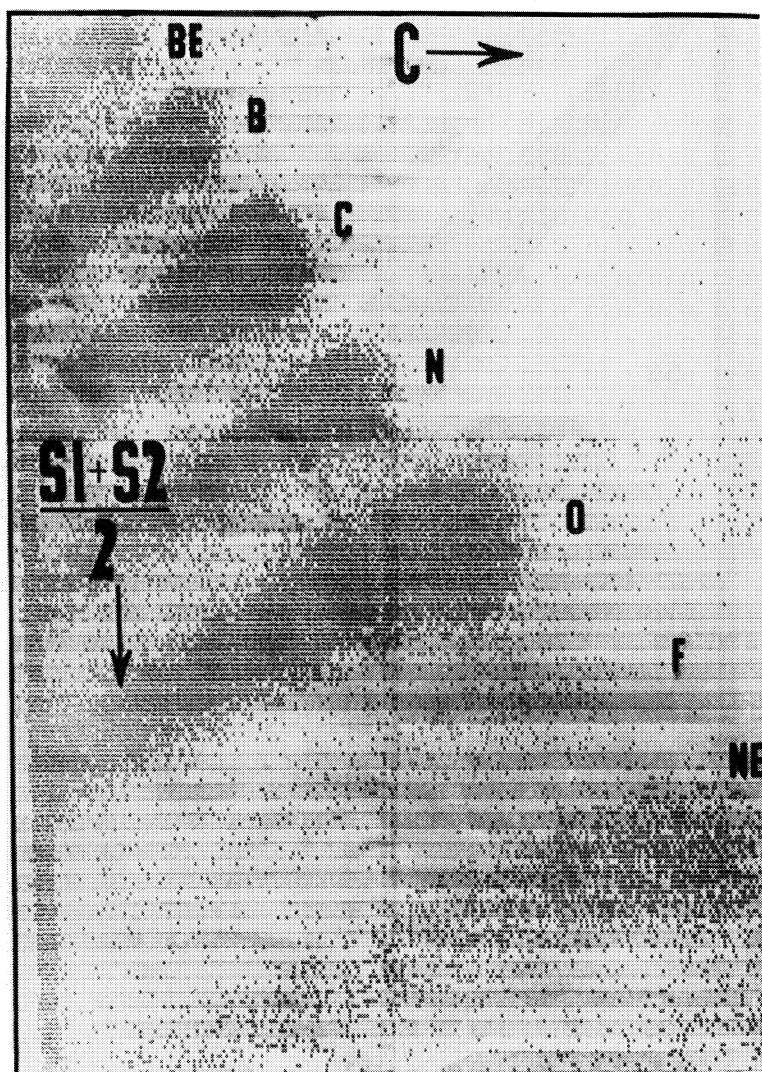

Fig. 3.—Matrix of events (S1 + S2)/2 versus C for the charge region $3 \leq Z \leq 8$ with selection criterion applied

event matrix with axes (S1 + S2)/2 versus C, subject to the above criterion, is shown in Figure 3.

For studies involving the gas Cerenkov detector a somewhat different procedure is used. First an S1 versus C matrix was formed subject to (1) an S1, S2 consistency criterion with $X = 0.4$ and (2) a gas detector criterion: $G(Z) > 0.3 \, G_{max}(Z)$ [$G_{max}(Z)$ is the maximum ($\beta = 1$) output of the gas detector as a function of the charge Z of the traversing nuclei]. On these plots both the C and S1 detectors are effectively at their high-energy values, and each charge appears as a well-resolved ellipse-shaped region. The parameters specifying the ellipses for each charge may be determined and utilized in the subsequent analysis.

Next for each charge from boron to silicon, plots of the individual banks of the gas detector G1 and G2 are combined in a matrix of $G1 - G2$ versus $G1 + G2$ for each charge region specification in S1 and C coordinates as discussed above. These plots are used to obtain pulse height distributions of the total signal from the gas Cerenkov detector ($G = G1 + G2$) for each charge subject to a G1, G2 consistency criterion which requires that G1 and G2 agree within 3 σ. These plots are also used to determine the sources of broadening to be removed from these pulse height distributions in the process of extracting the underlying energy spectra. A sample matrix of $G1 - G2$ versus $G1 + G2$ events for O nuclei is shown in Figure 4. This matrix is used to form the pulse height distribution of O nuclei above the gas Cerenkov threshold shown in Figure 6b.

The two dominant sources of broadening of the pulse height distributions, photoelectron fluctuations and path-length variations, are easily separated by an examination of the $G1 - G2$ versus $G1 + G2$ matrices. Photoelectron fluctuations produce uncorrelated fluctuations in the two separate banks of photomultiplier tubes and may be determined by examining pulse height distributions in the $G1 - G2$ dimension corresponding to narrow intervals in the $G = G1 + G2$ dimension. It is found that the full width at half-maximum of these fluctuations varies as the square root of the G signal level, as anticipated. The path-length fluctuations produce correlated fluctuations in the two separate photomultiplier tube banks, and the nature of these fluctuations was reproduced through Monte Carlo simulation.

b) Determination of Charge Abundances

For the solid Cerenkov detector, events in the (S1 + S2)/2 versus C matrix lie at a location dependent on their charge and velocity through the relationships

$$S = K_S \frac{Z^2}{\beta^2} f(Z, \beta) \quad \text{and} \quad C = K_C Z^2 \left(1 - \frac{\beta_0^2}{\beta^2}\right).$$

(3)

For each even charge the mean location of the charge

line on this matrix is first determined by visual inspection. This line is characterized by two endpoints (C_{max}, S_{min}) and ($C = 0, S_{max}$). The details of the response determined in the Cerenkov dimension are discussed more fully in the next section; therefore, it is sufficient to note at this point that the Cerenkov response is accurately represented by equation (3) and is calibrated by the locations of the C_{max} values corresponding to $\beta = 1$ particles of different charge. Thus the calculated Cerenkov output for particles of various Z and β and the observed pulse-height channel scale in an accurately known way in the Cerenkov dimension. It is therefore possible, using the smoothed charge lines and comparing pulse heights along these charge lines in the S dimension with the corresponding calculated value of energy loss $S \equiv (S1 + S2)/2$, to determine the function $f(Z, \beta)$ which includes the saturation effects in the scintillators for each even charge. At the same time a series of charge histograms for various intervals in C/C_{max} is constructed for each charge. These histograms are used initially to test the goodness of fit of the charge lines, along with the requirement that the variation of $f(Z, \beta)$ must behave in a systematic way with charge and energy. The location of the charge line is then fine tuned until an optimum goodness of fit is obtained and the residuals of the systematic behavior of the lines as a function of Z and β are a minimum. These constitute the best-fit charge lines from which the final charge histograms are obtained. The charge lines used for odd nuclei are a simple weighted average of the charge lines of the two adjacent even nuclei. Charge histograms are constructed for several intervals in C/C_{max}, and in Figure 5a we show such a histogram for $C/C_{max} > 0.6$. The charge composition in various broad energy ranges may then be determined from a series of these histograms. The procedure used is to first assume that each charge distribution is Gaussian in nature characterized by a σ. These Gaussian distributions are fitted to each individual charge distribution and adjusted in amplitude and σ so as to provide a best fit to the overall charge histogram. The σ derived for the interval $C/C_{max} > 0.6$ is equal to 0.23 charge units for Mg, 0.30 charge units for S, 0.32 charge units for Ca, and 0.40 charge units for Fe.

The actual charge abundances are determined to an accuracy that depends on the charge resolution, on the abundance of adjacent charges, and on the statistics of a given charge. As long as the resolution and the abundance of adjacent charges is such that the contribution of the more abundant adjacent (even) charges at the peak of the intermediate (odd) charge is negligible, then the flux of this intermediate charge is essentially known to the statistical accuracy of the data available. This situation exists for the odd nuclei F, Na, and Al and for several of the odd nuclei with $Z = 15-25$. The exceptions are P, Cl, and Mn, all of which lie near a much more abundant even nucleus. The most severely contaminated of these nuclei is Mn, where the contribution from Fe is ~40% of the total number of Mn nuclei at the peak of the Mn distribution—introducing an additional uncertainty
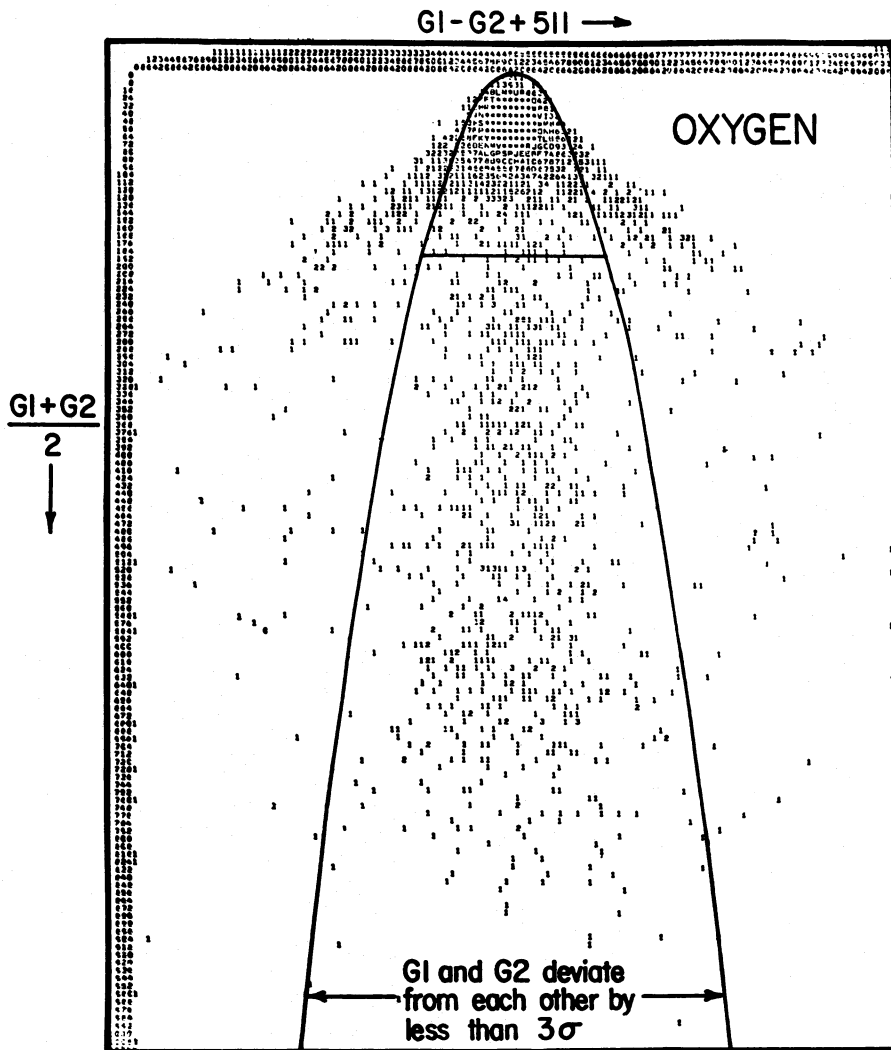
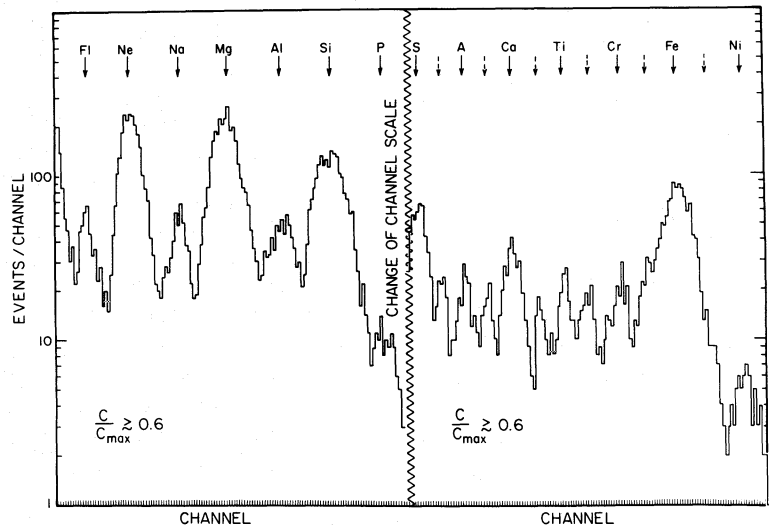FIG. 4.—Matrix of events G1 − G2 versus G1 + G2 for O nuclei with selection criterion applied

FIG. 5a.—Charge histogram in the interval $C/C_{max} \geq 0.6$ from UVT Lucite counter

of $\pm 20\%$ over that for statistics alone on the derived Mn abundance.

In order to optimize charge resolution for the gas Cerenkov detector, the signals from S1, C1 and from S1, C1, C2 were used for the 1974 and 1976 data, respectively. A multidimensional plot of these detector outputs for $G(Z) > 0.3\, G_{max}(Z)$ yields ellipsoidal distributions which can be transformed to multidimensional spherical distributions with a suitable transformation. One then determines a space curve which passes through the center of each of these distributions for each charge; and one also determines a function specifying charge in terms of the length along this curve from a suitable origin. Finally the charge for a given event is obtained by dropping an orthogonal line from the multidimensional coordinates of the event to the space curve, which then determines a point on the curve and a corresponding value of the charge Z (not necessarily integer). The number of events for each charge Z above the energy threshold corresponding to $G(Z) > 0.3\, G_{max}(Z)$ may then be determined by summing counts from $Z - 0.5$ to

$Z + 0.5$. Smaller intervals for the odd charges are used when necessary together with suitable charge overlap corrections. In Figure 5b we show the charge histogram obtained for the above analysis for the 1976 data. The σ derived from these data is 0.18 charge units for O nuclei, 0.20 charge units for Si nuclei, and 0.31 charge units for Fe nuclei.

VI. DERIVATION OF THE ENERGY SPECTRA OF INDIVIDUAL NUCLEI

a) The UVT Lucite Counter

The background-corrected $(S1 + S2)/2 \times C$ matrices are the basic ones upon which the data analysis is carried out and the spectral information unfolded. The Cerenkov distributions for the individual charges are used to unfold the particle energy spectra. Examples of these Cerenkov distributions for C, Si, and Fe nuclei in the UVT Lucite counter are shown in Figure 6a.

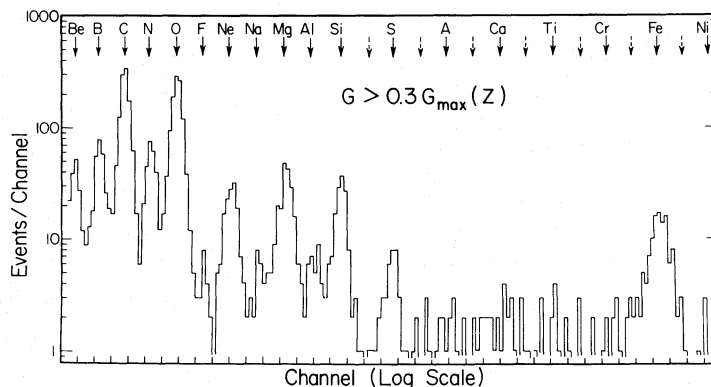The procedure for unfolding the energy spectra from the pulse height distributions has recently been

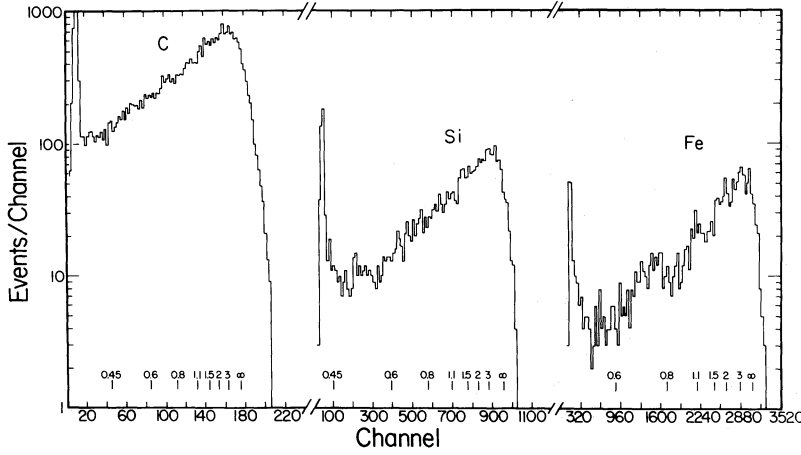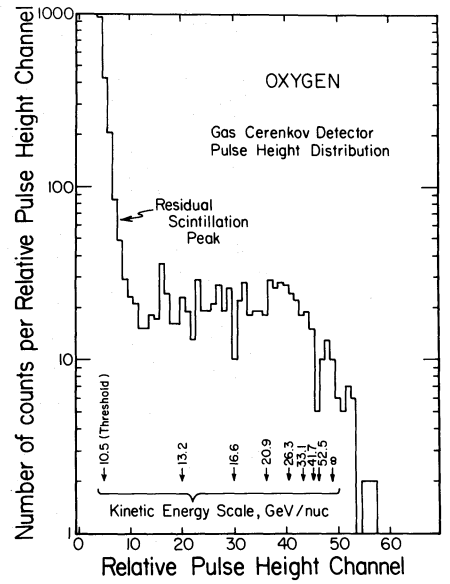FIG. 5b.—Charge histogram in the interval $G/G_{max} \geq 0.3$ from the Freon Gas Cerenkov counter

FIG. 6a.—Cerenkov distributions for C, Si, and Fe nuclei showing location of energy interval boundaries for UVT Lucite counter.
FIG. 6b.—Cerenkov distribution for O nuclei from Freon gas Cerenkov counter, 1974.

discussed by Lezniak (1975). He presents two approaches: one is a simplified graphical approach utilizing graphs showing the corrections to the raw data necessary to convert the observed pulse height distribution into energy spectra; the other is a formal deconvolution of the Cerenkov pulse-height distribution. We have used the simplified graphical approach for unfolding the spectra from the UVT Lucite counters. The graphs presented by Lezniak for this correction are obtained directly from a formal convolution calculation using various input spectra and instrumental resolutions.

Recall that the dependence of the Cerenkov light on the energy E of the incident nucleus may be written

$$C = K_C Z^2 \left(1 - \frac{\beta_0^2}{\beta^2}\right) = C_{max} \frac{1 - \beta_0^2/\beta^2}{1 - \beta_0^2}, \qquad (4)$$

where β_0 is the threshold velocity which is 0.66 for our Cerenkov detector, which has an effective index of refraction of 1.51. The first step in the determination of an energy spectrum is to determine the value of $C_{max} = K_C Z^2 \cdot (1 - \beta_0^2)$ corresponding to $\beta = 1$ nuclei for each charge. This quantity is determined from the individual Cerenkov histograms for each charge using the procedure outlined by Lezniak. This quantity is dependent on the resolution of the Cerenkov detector, which in turn is determined by the essentially Gaussian photoelectron statistics in the Cerenkov detector.

The relationship between C_{max} and the observed peak in the pulse height distribution C_{obs} is given in Figure 4 of Lezniak (1975) for various input spectra and resolutions. The FWHM resolution for each charge may be found from the actual pulse-height

distributions for each charge, as outlined by Lezniak and summarized in his Figures 5 and 6. In our Figure 7 we show the quantity $\Delta C_{max} \equiv C_{max}(Z + 2) - C_{max}(Z)$ obtained for each charge from the combined flight data. Also shown in this figure is the FWHM Cerenkov resolution determined for $\beta = 1$ particles of each charge. Note that both ΔC_{max} (and hence C_{max}) and the FWHM for each charge vary in a systematic way, so the accuracy of these quantities for each charge is higher than the accuracy for each charge independently. We estimate that the pulse height of C_{max} can be located to an accuracy of $\lesssim 1\%$
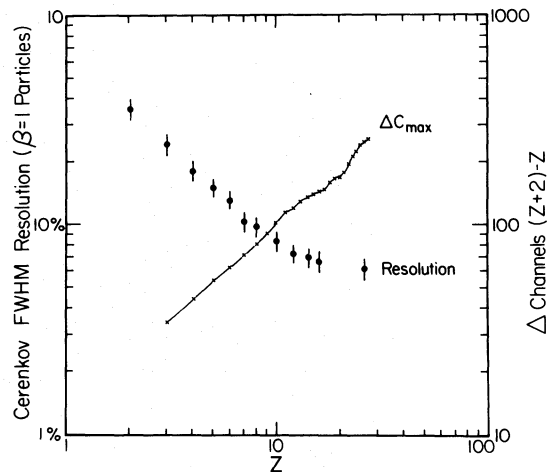

FIG. 7.—$C_{max}(Z + 2) - C_{max}(Z)$ and FWHM resolution for $\beta = 1$ particles of each charge Z as derived from the UVT Lucite counter.
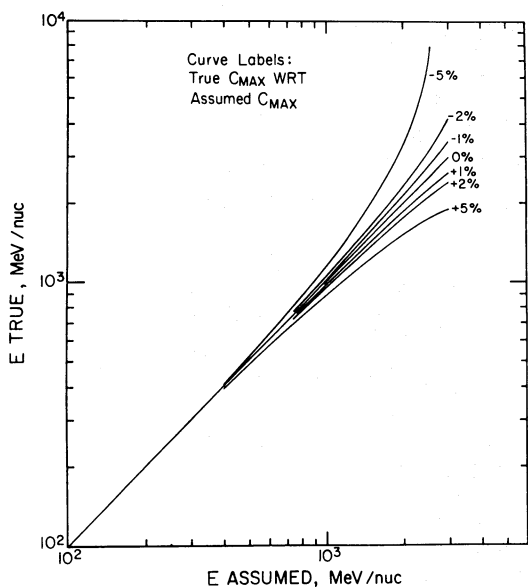
FIG. 8.—Error introduced in the energy interval boundaries as a result of an error in C_{max}.

for each charge with $Z \leq 14$. This uncertainty in C_{max} translates into an uncertainty in the energy associated with the boundaries of the different energy intervals. Figure 8 shows the error introduced in the energy interval boundaries as a function of the error in the location of C_{max}. The energy uncertainty in the energy interval boundaries is negligible at the lower energies. This uncertainty, along with statistical fluctuations in the data set, ultimately determines the highest energy to which the spectrum can be accurately unfolded.

Basically the location of the C_{max} point determines the energy scale of each charge through equation (4). However, δ rays produced by the particle modify this response slightly. Lezniak (1976) has calculated this effect as a function of Z and β, and for different

values of n, the index of refraction, and we have adjusted our energy scale for this effect. The final energy interval boundaries are chosen for each charge as illustrated for C, Si, and Fe nuclei in Figure 6a.

The basic quantity that is measured is the number of events $N_m(\Delta E)$ that fall into a certain energy bin ΔE. This quantity is related to the quantity $N(E)$, the true number of events in the energy interval ΔE. This relationship may be written

$$N(\Delta E) = N_m(\Delta E) \times F, \qquad (5)$$

where F is a correction factor depending on (1) the energy interval, (2) the resolution, and (3) the spectrum. If the instrumental resolution is much less than the interval width E, then $F \sim 1$, and the correction is essentially independent of the spectrum. This situation applies for most nuclei for energies ≤ 800 MeV per nucleon in the UVT Lucite counter. At higher energies, there is a nonsymmetrical feeding of events from one energy bin to another which influences F. The calculation of F is discussed by Lezniak (1975). This detailed analysis is summarized in Figure 9a, which shows the values of the percent correction $100(F-1)$ as a function of FWHM Cerenkov resolution and the kinetic energy for the nominal (helium) spectrum given in Figure 10. Since the resolution α of our counter is generally less than 0.3 (FWHM = 30%) for all Z, the deconvolution corrections are $\leq \pm 10\%$ for all nuclei (at all energies up to ~ 2 GeV per nucleon). Lezniak (1977) has produced additional graphs similar to Figure 9a for a variety of different high-energy spectral indices. As long as the resolution is less than 0.3, the adjustments for different high-energy spectra also remain $\leq \pm 10\%$ up to ~ 2 GeV per nucleon. In other words, if the resolution is good enough, the true spectrum may be derived from the pulse-height distribution itself with little error up to ~ 2 GeV per nucleon, independent of the shape of the high-energy spectrum. As a result of this independence on spectral shape, we have
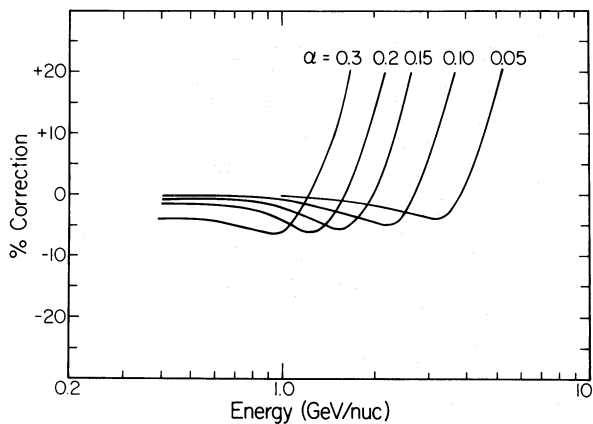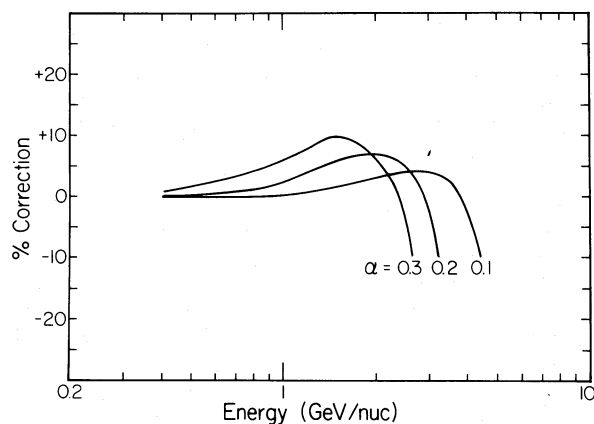

FIG. 9a.

FIG. 9b.

FIG. 9a.—Values of the deconvolution correction factor F [plotted here as $100(F-1)$] as a function of the kinetic energy and the Cerenkov resolution α for a nominal input spectrum.

FIG. 9b.—Values of the deconvolution correction factor for the integral intensities as a function of energy and Cerenkov resolution.
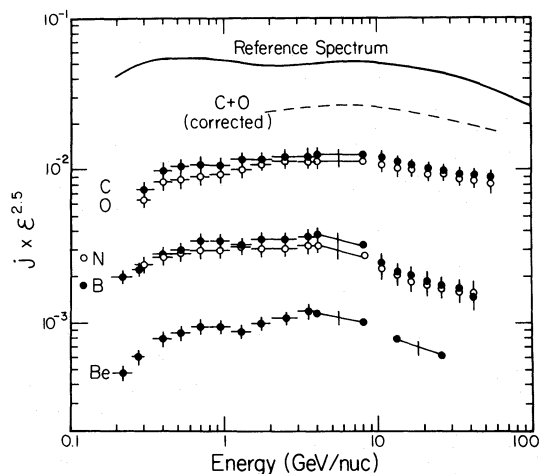
FIG. 10.—Energy spectra for Be, B, C, N, and O nuclei. Shown is the nominal spectrum taken for the deconvolution of the UVT Lucite counter data. The source spectrum for C + O nuclei, corrected for energy-dependent path-length variations, is also shown.

adopted a nominal high-energy spectrum $E^{-2.6}$ (see Fig. 10) as a first approximation for the deconvolution correction for all charges—even though the actual high-energy spectra may be somewhat different for each charge. Above 2 GeV per nucleon both the error in the energy interval itself and the dependence on the assumed high-energy spectra rapidly become appreciable. Thus we have taken 4 GeV per nucleon as a reasonable upper limit to the energy range in which accurate spectral information can be unfolded from the UVT Lucite Cerenkov detector by requiring that the differential and integral spectra at 4 GeV per nucleon be continuous (see eq. [9] below; see also discussion of high-energy limit by Lezniak 1975). A very similar approach to the unfolding of the energy spectrum from the pulse-height distribution in a solid Cerenkov counter has been recently carried out by Maehl *et al.* (1976).

For each charge, then, we have the differential spectra up to 4 GeV per nucleon plus an integral point at greater than 4 GeV per nucleon. This integral point is important for the analysis since it shows the self-consistency of the spectra derived. To obtain this point we have used the convolution procedures of Lezniak and again expressed the correction to the observed integral flux in graphical form, as shown in Figure 9b, for different resolutions α, and for the nominal spectrum. As pointed out earlier, all differential and integral spectral points are initially determined using the corrections based on the nominal spectrum. If the derived spectra for any charge differ significantly from this standard spectrum, a new input spectrum is chosen which matches the derived spectrum and a new set of corrections is obtained, leading to a new derived spectrum. This iterative procedure is followed until the derived and input spectra agree. This iteration affects only the originally derived points above ~2 GeV per nucleon and the integral point.

It is of great importance, in terms of the accuracy of the spectra derived from the UVT Lucite Cerenkov counter, to note that the possible choice of the differential spectra above ~4 GeV per nucleon are greatly constrained by the integral flux derived at 4 GeV per nucleon and the integral and differential fluxes ≥10.5 GeV per nucleon derived simultaneously from the gas Cerenkov counter. This use of Cerenkov counters in tandem greatly improves the accuracy with which the spectrum can be derived using deconvolution techniques from the lower threshold counter.

b) The Gas Cerenkov Counter

In this paper the data from the gas Cerenkov detector are analyzed to provide differential spectra for the charges $Z = 5$–14 from the Sioux Falls 1974 data, and integral spectra for the charges $Z = 4$–28 from an analysis of the Sioux Falls 1974 and 1976 data.

The relevant two-dimensional integral equation to be solved to extract an energy spectrum from the gas Cerenkov detector pulse height distribution for a given charge component is as follows:

$$f(x) = G \int_{x'} F(x, x') \left\{ \int_{x''} E(x', x'') j[T(x'')] dx'' \right\} dx' ,$$

$$(6)$$

where the pulse-height distribution is given by $f(x)$, the kinetic energy spectrum by $j(T)$, the redistribution functions for path-length variations and photoelectron variations by $E(x', x'')$ and $F(x, x')$ respectively, and the geometric factor of the experiment by G. The pulse-height-channel–kinetic-energy correspondence $x(T)$ and its inverse function $T(x)$ were determined from theoretical calculations of the scintillation light and the Cerenkov light produced both directly by the incident particle and indirectly through knock-on electrons. The relative amount of scintillation light was determined via cross plots of the output of the solid (C) and gas (G) Cerenkov detectors.

The order of integration in the above integral equation may be inverted to obtain the following one-dimensional integral equation:

$$f(x) = \int_{x''} H(x, x'') j[T(x'')] dx'' ,$$

$$(7)$$

where the kernel $H(x, x'')$ is given by the equation

$$H(x, x'') = G \int_{x'} F(x, x') E(x', x'') dx' . \qquad (8)$$

This one-dimensional integral equation may be solved as discussed in § 3 of Lezniak (1975) to extract the kinetic energy spectrum $j[T(x)]$. The path-length distribution function $E(x', x'')$ is a triangular-shaped distribution when plotted as a function of x'/x''. This distribution has a full width at half-maximum of 21% and 14% for the 1974 and 1976 versions of the gas Cerenkov detector, respectively. (The 1976 version made use of a thin baffle to narrow the path-length

distribution even though a wide angle of acceptance was utilized.) The photoelectron redistribution function $F(x, x')$ is a Gaussian in the variable x-x' with a half-width which is directly proportional to the square root of x'.

Two constraints were implemented in the full deconvolution solution of the above integral equation to obtain the differential spectra from the pulse-height distributions. The first is a smooth spectrum constraint which is a modification of that presented by Lezniak (1975) and ensures equal weighting of all spectral points in the derived spectrum. The second is an integral count constraint which ensures that the total number of counts in the observed pulse-height distribution is equal to that in the smoother pulse height distribution generated from the derived smooth spectrum.

Integral spectra were derived independently of the differential spectra and provided a cross check on each method, which demonstrated that the two methods are consistent with one another. In order to determine the integral number of counts above some common energy for all of the charges, a histogram as a function of Z was plotted for $G(Z) \geq 0.3 \, G_{max}(Z)$. The determination of charge was discussed earlier. This criterion on $G(Z)$ removes from consideration the large number of counts at low-G pulse-height channels which have energy below the gas Cerenkov threshold and excite the gas Cerenkov detector through scintillation light production exclusively. The resulting charge histogram from this analysis has been shown in Figure 5b.

VII. ATMOSPHERIC AND INSTRUMENTAL CORRECTIONS

Once the numbers of events in each energy interval have been determined using the appropriate deconvolution correction, it is further necessary to correct the data for the individual charges for nuclear interactions in the telescope as well as absorption and production in the overlying atmosphere. These corrections are shown separately in Table 2. The instrumental interaction correction is applied to the corrected intensities of nuclei that pass through the telescope without interaction, in order to obtain the intensities above the top of the first counter. The magnitude of this correction depends on the amount of material in the telescope down to the final element in the selection process used to derive the S × C matrices, in this case S2, which is 5.3 g cm^{-2} for the 1974 telescope and 8.7 g cm^{-2} for the 1976 telescope. These thicknesses must be multiplied by the efficiency with which interacting particles are detected by this selection criterion which is 85% ± 5%.

The atmospheric correction is based on a one-dimensional diffusion model through an atmospheric slab of 3.0 g cm^{-2} of air. This calculation makes use of the target factors presented by Lindstrom et al. (1975) to multiply the measured and semiempirical estimates of proton-nucleus cross sections. The relative cross sections in air and hydrogen scale in such a way that 3 g cm^{-2} of air is roughly equivalent

TABLE 2
INSTRUMENTAL AND ATMOSPHERIC CORRECTIONS
(1974 Data)

Charge	Instrument (5.3 g cm^{-2})	Air (3.0 g cm^{-2})	Total
Li.............	1.171	0.990	1.159
Be.............	1.182	0.980	1.158
B.............	1.198	1.010	1.210
C.............	1.207	1.094	1.321
N.............	1.217	1.036	1.261
O.............	1.228	1.117	1.372
F.............	1.239	1.030	1.276
Ne............	1.250	1.093	1.366
Na............	1.261	1.070	1.349
Mg............	1.273	1.133	1.442
Al.............	1.282	1.087	1.393
Si.............	1.292	1.151	1.487
S.............	1.310	1.215	1.474
$Z = 17$–19.....	1.330	1.072	1.426
Ca............	1.351	1.130	1.527
$Z = 21$–25.....	1.383	1.102	1.524
Fe............	1.438	1.225	1.761
Ni............	1.472	1.242	1.828

to 1.0–1.5 g cm^{-2} of interstellar hydrogen. Thus uncertainties of $\pm 20\%$, which are probably inherent in the cross sections in air, translate into errors of ± 0.2–0.3 g cm^{-2} in terms of path lengths in interstellar hydrogen.

Note that if these instrumental and atmospheric corrections are expressed relative to a particular charge, for example oxygen, they are significantly smaller (e.g., Juliusson 1974). Thus the relative intensities of the different nuclei can be determined to a greater precision than the absolute intensity.

VIII. RESULTS

a) Energy Spectra

The fully corrected data from the UVT Lucite Cerenkov counter is shown in Table 3 and that from the Freon gas Cerenkov counter is shown separately in Table 4. Spectra for the most important charges and groups of charges are shown in Figures 10 and 11. In these figures the differential intensities are multiplied by $\epsilon^{2.5}$, where ϵ = total energy. This procedure has the advantages of (1) visually enhancing any intensity differences between charges and (2) illustrating more clearly any spectral differences between the various charges. Note that in these figures the integral intensities are plotted as follows: The measured integral flux J_0 above a kinetic energy E_0 is related to the differential flux j_0 at the same energy by

$$j_0 = \frac{(\gamma - 1)J_0}{E_0}. \tag{9}$$

The value of γ is chosen so that j is continuous at E_0. The resulting differential spectrum is then shown as a line extending from E_0 to $2E_0$. This is the energy range over which typically two-thirds of the events in the integral spectrum lie and therefore where it is

TABLE 3

Spectral Data—UVT Lucite Cerenkov Detector

Energy Interval (GeV per nucleon)

Charge	0.35–0.45	0.45–0.60	0.6–0.8	0.8–1.1	1.1–1.5	1.5–2.0	2.0–3.0	3.0–4.0	>4.0
Be	(262) 0.041 ± 0.003	(320) 0.050 ± 0.003	(362) 0.057 ± 0.003	(388) 0.060 ± 0.003	(315) 0.048 ± 0.003	(279) 0.042 ± 0.003	(296) 0.051 ± 0.003	(226) 0.031 ± 0.002	(462)* 0.065 ± 0.003†
B	(805) 0.136 ± 0.005	(1010) 0.169 ± 0.005	(1239) 0.208 ± 0.006	(1314) 0.219 ± 0.006	(1039) 0.170 ± 0.005	(926) 0.152 ± 0.005	(934) 0.160 ± 0.005	(523) 0.086 ± 0.004	(1461) 0.204 ± 0.006
C	(2514) 0.463 ± 0.010	(3500) 0.644 ± 0.013	(3672) 0.676 ± 0.013	(3755) 0.687 ± 0.013	(3339) 0.610 ± 0.012	(2783) 0.500 ± 0.011	(3112) 0.561 ± 0.011	(1652) 0.315 ± 0.009	(4680) 0.881 ± 0.016
N	(740) 0.130 ± 0.005	(909) 0.159 ± 0.005	(935) 0.164 ± 0.005	(1006) 0.175 ± 0.006	(982) 0.169 ± 0.006	(729) 0.124 ± 0.005	(774) 0.132 ± 0.005	(455) 0.081 ± 0.004	(1065) 0.182 ± 0.006
O	(2198) 0.413 ± 0.009	(2831) 0.538 ± 0.011	(3012) 0.578 ± 0.012	(3132) 0.596 ± 0.012	(2922) 0.532 ± 0.011	(2524) 0.468 ± 0.010	(2925) 0.535 ± 0.011	(1570) 0.313 ± 0.009	(4107) 0.823 ± 0.016
F		(78) 0.016 ± 0.002	(72) 0.015 ± 0.002	(90) 0.019 ± 0.002	(72) 0.014 ± 0.002	(70) 0.013 ± 0.002	(58) 0.011 ± 0.002	(27) 0.005 ± 0.001	(64) 0.012 ± 0.002
Ne		(430) 0.082 ± 0.004	(487) 0.093 ± 0.004	(511) 0.097 ± 0.004	(484) 0.091 ± 0.004	(346) 0.065 ± 0.004	(432) 0.080 ± 0.004	(267) 0.053 ± 0.003	(633) 0.124 ± 0.004
Na		(72) 0.014 ± 0.002	(89) 0.018 ± 0.002	(93) 0.019 ± 0.002	(90) 0.018 ± 0.002	(83) 0.016 ± 0.002	(80) 0.016 ± 0.002	(39) 0.008 ± 0.002	(67) 0.013 ± 0.002
Mg		(533) 0.107 ± 0.004	(582) 0.117 ± 0.004	(614) 0.123 ± 0.004	(581) 0.115 ± 0.004	(505) 0.105 ± 0.004	(565) 0.110 ± 0.004	(303) 0.053 ± 0.003	(651) 0.128 ± 0.004
Al		(90) 0.019 ± 0.002	(110) 0.023 ± 0.002	(98) 0.020 ± 0.002	(100) 0.021 ± 0.002	(91) 0.018 ± 0.002	(103) 0.021 ± 0.002	(56) 0.012 ± 0.002	(97) 0.021 ± 0.002
Si		(336) 0.071 ± 0.004	(390) 0.081 ± 0.004	(420) 0.087 ± 0.004	(397) 0.082 ± 0.004	(355) 0.072 ± 0.004	(404) 0.081 ± 0.004	(236) 0.051 ± 0.003	(493) 0.105 ± 0.004
S		(71) 0.015 ± 0.002	(102) 0.021 ± 0.002	(104) 0.022 ± 0.002	(96) 0.020 ± 0.002	(80) 0.016 ± 0.002	(92) 0.019 ± 0.002	(52) 0.011 ± 0.002	(98) 0.022 ± 0.002
17–19		(81) 0.016 ± 0.002	(106) 0.022 ± 0.002	(105) 0.021 ± 0.002	(108) 0.022 ± 0.002	(97) 0.020 ± 0.002	(84) 0.017 ± 0.002	(40) 0.008 ± 0.002	(97) 0.022 ± 0.002
Ca		(46) 0.011 ± 0.002	(68) 0.014 ± 0.002	(72) 0.015 ± 0.002	(50) 0.010 ± 0.002	(47) 0.010 ± 0.020	(58) 0.012 ± 0.002	(30) 0.006 ± 0.001	(62) 0.013 ± 0.002
21–25		(143) 0.031 ± 0.003	(170) 0.036 ± 0.003	(162) 0.034 ± 0.003	(167) 0.035 ± 0.003	(148) 0.032 ± 0.003	(167) 0.035 ± 0.003	(94) 0.021 ± 0.002	(142) 0.032 ± 0.003
Fe		(212) 0.052 ± 0.004	(234) 0.057 ± 0.004	(218) 0.053 ± 0.004	(201) 0.054 ± 0.004	(241) 0.059 ± 0.004	(240) 0.058 ± 0.04	(157) 0.043 ± 0.003	(300) 0.086 ± 0.005
Ni		(13) 0.003 ± 0.001	(10) 0.002 ± 0.001	(18) 0.005 ± 0.001	(13) 0.003 ± 0.001	(11) 0.003 ± 0.001	(12) 0.003 ± 0.001	(5) 0.001 ± 0.005	(11) 0.003 ± 0.001

* Number of events.
† Fluxes in particles $m^2 \, sr^{-1} \, s^{-1}$.

688

TABLE 4

INTEGRAL AND DIFFERENTIAL INTENSITIES GREATER THAN 10 GeV PER NUCLEON

CHARGE	>10.5	>13.1	KINETIC ENERGY (GeV per nucleon)							
			10.48	13.19	16.61	20.91	26.32	33.14	41.72	52.52
Be..........	(98)* 1.48 ± 0.16†									
B..........	(250) 3.62 ± 0.23	(131) 2.17 ± 0.19	5.35 ± 0.55‡	2.90 ± 0.29	1.57 ± 0.15	0.85 ± 0.07	0.46 ± 0.035	0.25 ± 0.03	0.14 ± 0.03	...
C..........	(1110) 19.3 ± 0.62	(695) 12.5 ± 0.48	27.6 ± 1.2	15.2 ± 0.70	8.34 ± 0.34	4.59 ± 0.17	2.53 ± 0.09	1.40 ± 0.05	0.77 ± 0.05	0.43 ± 0.05
N..........	(236) 3.68 ± 0.24	(130) 2.24 ± 0.20	4.91 ± 0.51	2.69 ± 0.27	1.47 ± 0.14	0.81 ± 0.07	0.44 ± 0.035	0.24 ± 0.03	0.14 ± 0.03	...
O..........	(1015) 18.7 ± 0.59	(627) 11.8 ± 0.47	24.6 ± 1.1	13.7 ± 0.6	7.61 ± 0.32	4.23 ± 0.16	2.35 ± 0.08	1.30 ± 0.05	0.72 ± 0.05	0.39 ± 0.05
F + Na + Al	(77) 1.29 ± 0.15	(58) 0.89 ± 0.16	1.87 ± 0.34	...	0.59 ± 0.08	...	0.19 ± 0.38	...	...	...
Ne..........	(132) 2.48 ± 0.21	(105) 1.96 ± 0.19	12.4 ± 0.8	6.95 ± 0.45	3.91 ± 0.23	2.20 ± 0.12	1.24 ± 0.06	0.70 ± 0.05	0.39 ± 0.05	...
Mg..........	(184) 3.64 ± 0.27	(118) 2.33 ± 0.21								
Si..........	(139) 2.91 ± 0.25	(91) 1.85 ± 0.19								
S..........	(34) 0.67 ± 0.12	(19) 0.29 ± 0.08								
17–19..........	(30) 0.59 ± 0.11	(18) 0.33 ± 0.09								
Ca..........	(24) 0.51 ± 0.10	(19) 0.39 ± 0.09								
21–25..........	(53) 1.21 ± 0.17	(35) 0.68 ± 0.12								
Fe..........	(109) 2.92 ± 0.28	(74) 1.78 ± 0.21								
Ni..........	(4) 0.11 ± 0.06	(4) 0.10 ± 0.05								

* Number of events.
† Integral fluxes in units of 10^{-2} particles m^{-2} sr^{-1} s^{-1}.
‡ Differential fluxes in units of 10^{-6} particles m^{-2} sr^{-1} per MeV per nucleon.
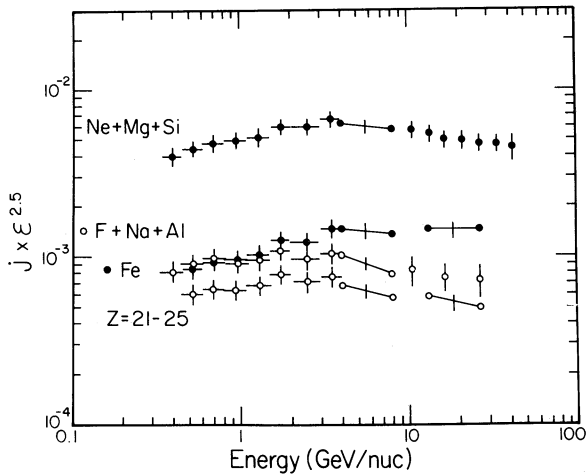
689

FIG. 11.—Energy spectra for (Ne + Mg + Si), (F + Na + Al), $Z = 21$–25, and Fe nuclei.

FIG. 12.—Abundance ratios of (Be + B)/C and N/O nuclei. Dashed curves are for propagation through 5 g cm^{-2} of interstellar hydrogen. C3 is from Garcia Munoz, Mason, and Simpson 1977b. Points labeled X are from $dE/dx \times E$ measurements.

most sensitive to the differential spectrum. Notice that, in general, the differential spectrum derived from the integral flux data above 4 GeV per nucleon connects well to the spectra measured with the gas Cerenkov counter.

Table 5 shows the best-fit spectral indices we have derived for various charges from the integral data at 2.0 and 13.1 GeV per nucleon.

b) Charge Ratios

In many applications and in the interpretation of the data it is sometimes easier to examine the spectral differences between charges by comparing the relative abundances of the different nuclei as a function of energy. In Figures 12 and 13 we show ratios of various secondary-to-primary (source) nuclei as a functio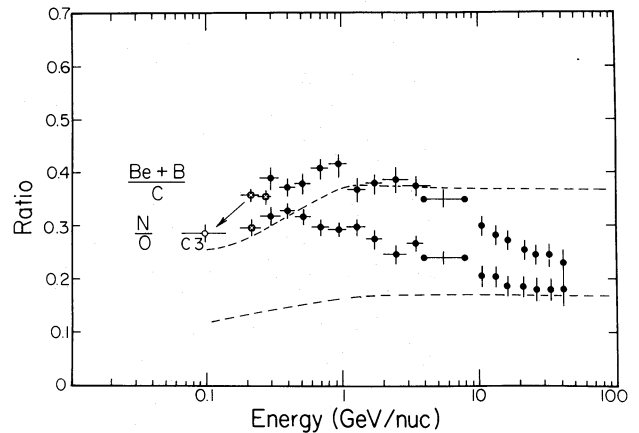n of energy. In Figures 14 and 15 we show the ratios of the intensities of various primary nuclei as a function of energy.

All of these figures illustrate the behavior discussed in the Introduction, namely: (1) When comparing any mainly secondary nucleus with the nearest heavier primary nucleus, the ratio is seen to decrease as one goes to higher energies. This decrease is evident in all of the data above ~ 1 GeV per nucleon, although the decrease is somewhat less than reported in some of the earlier results. Below ~ 1 GeV per nucleon the ratios become flat and even appear to decrease at the lower energies. Above 1 GeV per nucleon, where interplanetary energy loss effects are small and the fragmentation parameters are nearly independent of energy, these data may be interpreted directly in terms of a decreasing material path length X for fragmentation into the secondary nuclei. Below ~ 1 GeV per

TABLE 5

Spectral Indices based on Integral Intensities > 2.0 and 13.1 GeV per
Nucleon Kinetic Energy

| Charge	Ratio $J(2.0)/J(13.1)$	Kinetic Energy γ	Total Energy γ
He*	13.2 ± 0.6	2.37 ± 0.06	2.65 ± 0.07
B	24.8 ± 2.2	2.71 ± 0.05	3.06 ± 0.06
C	14.9 ± 0.6	2.43 ± 0.02	2.74 ± 0.02
N	19.3 ± 1.7	2.57 ± 0.04	2.89 ± 0.5
O	14.8 ± 0.6	2.43 ± 0.02	2.72 ± 0.02
F + Na + Al	14.4 ± 2.9	2.42 ± 0.11	2.70 ± 0.12
Ne	13.2 ± 1.4	2.37 ± 0.06	2.65 ± 0.07
Mg	13.4 ± 1.3	2.38 ± 0.06	2.66 ± 0.07
Si	13.2 ± 1.5	2.37 ± 0.06	2.65 ± 0.07
S	17.0 ± 4.5	2.51 ± 0.13	2.81 ± 0.14
17–19	13.7 ± 4.1	2.39 ± 0.16	2.67 ± 0.17
Ca	8.5 ± 2.3	2.13 ± 0.13	2.37 ± 0.14
21–25	13.0 ± 2.7	2.36 ± 0.12	2.64 ± 0.13
Fe	10.0 ± 1.2	2.23 ± 0.07	2.47 ± 0.08

* Based on Webber and Lezniak 1974.
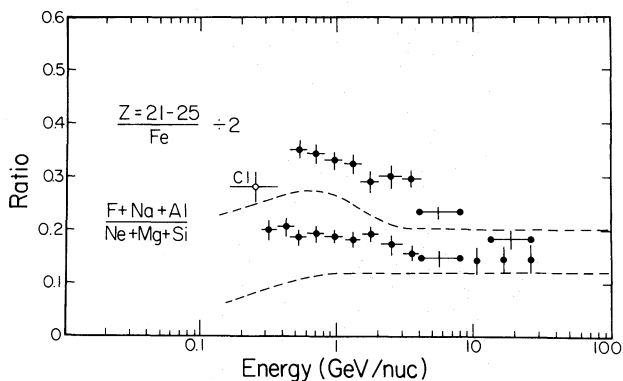
FIG. 13.—Abundance ratios of (F + Na + Al)/(Ne + Mg + Si) and (Z = 21–25)/Fe nuclei. Dashed curves are for propagation through 5 g cm^{-2} of interstellar hydrogen. C1 is from Garcia Munoz, Mason, and Simpson 1977a.

nucleon the effects are more complicated, as will be discussed shortly. (2) When comparing the ratio of any primary nucleus with a heavier primary nucleus, one sees that the ratio decreases as one goes to higher energies. Again this decrease is evident in all of the data above ~1 GeV per nucleon, while below this energy these ratios also become flat or decrease. A model in which the path length decreases with energy can also explain this behavior above 1 GeV per nucleon, as will, of course, any basic differences in the original accelerated spectra of these primary nuclei.

IX. DISCUSSION OF THE RESULTS

We shall interpret these results in terms of the interstellar propagation model that has been most widely used in explaining previous cosmic-ray composition measurements. This is the so-called leaky-box
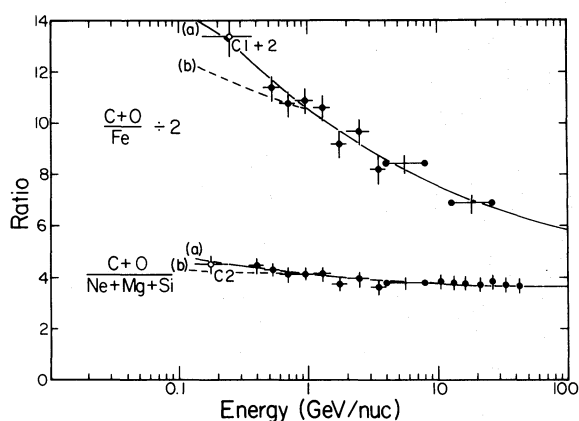

FIG. 14.—Abundance ratios of (C + O)/(Ne + Mg + Si) and (C + O)/Fe nuclei. Predicted ratios based on observed path-length dependence with energy are shown as solid curves. Curve (a) is for path length ~$E^{-0.3}$ below 1 GeV/nuc. Curve (b) is for path length independent of energy. C1 and 2 is from Garcia Munoz, Mason, and Simpson 1977a and Garcia Munoz et al. 1977.
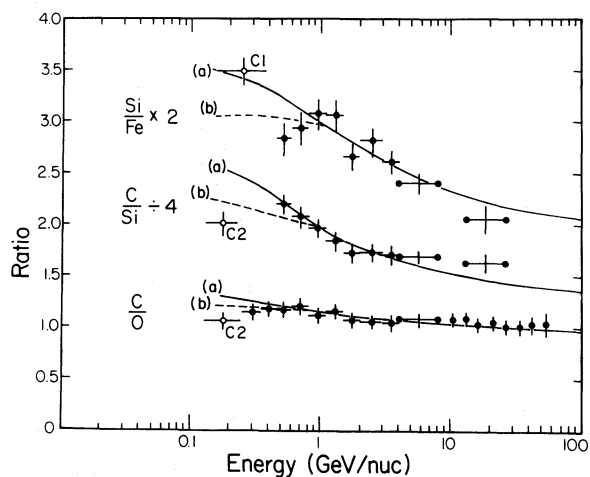

FIG. 15.—Abundance ratios of C/O, C/Si, and Si/Fe nuclei. Predicted ratios based on observed path-length dependence with energy are shown as solid curves. Curve (a) is for path length ~$E^{-0.3}$ below 1 GeV per nucleon. Curve (b) is for path length independent of energy.

model (Cowsik et al. 1965) in which the cosmic-ray transport is characterized by an escape length $\langle X \rangle$ in grams cm^{-2}. The distribution of path lengths in this model is an exponential ($e^{-(X/\langle X \rangle)}/\langle X \rangle$) with a characteristic path length $\langle X \rangle$. During this propagation the cosmic-ray composition is altered in the interstellar medium by fragmentation, ionization energy loss, and scattering in the galactic magnetic fields. The interstellar calculation is performed by setting up an initial source distribution and integrating stepwise the cosmic-ray transport equation. At each step the fragmentation, radio nuclide decay, and energy loss of the particles are calculated. Initially we take a set of previously determined source abundances (Shapiro and Silberberg 1975) and calculate the corresponding abundances outside of the heliosphere. For this calculation we assume an exponential path-length distribution with a characteristic path length $\langle X \rangle = 5$ g cm^{-2} as established by earlier studies at lower energies. The interstellar fragmentation parameters are based on those used by Fontes (1977). We also assume that the source spectra of all primary nuclei are identical. Later we assume that the escape length has a dependence on kinetic energy E given by $X(E) = X_0 E^{-\alpha}$. We also examine the effects of taking different initial energy spectra for the primary nuclei, and the influence of interplanetary modulation on the results. Finally we derive a new set of source abundances providing a best fit to the measured abundance data at all energies.

a) Secondary-to-Primary Nucleus Ratios

The secondary-to-primary nuclei ratios are most sensitive to the escape length and its possible variation with energy, so we begin by showing in Figures 12 and 13 the expected ratios for propagation through an exponential path length distribution with a characteristic path length $\langle X \rangle = 5$ g cm^{-2} of interstellar
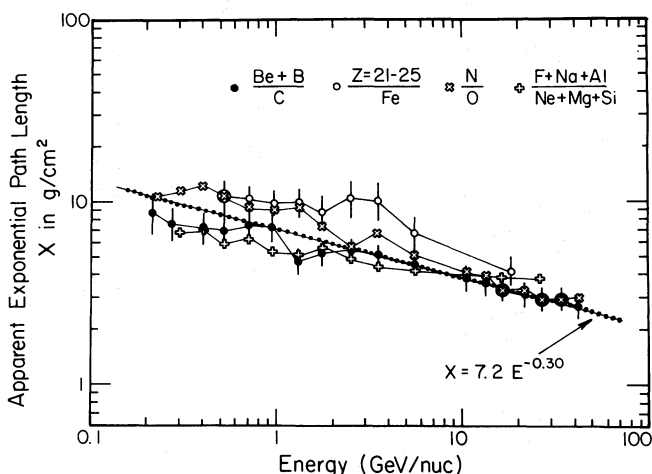
Fig. 16.—Apparent path length as a function of energy as derived from various secondary-to-primary ratios. Assumed source abundances for secondary components are discussed in text.

material. It is clear that this constant escape length provides a poor fit to the data. Also the implied path length at a given energy is much greater than 5 g cm^{-2} for the N/O and (F + Na + Al)/(Ne + Mg + Si) ratios, indicating that these secondary nuclei have a source component, as is well known. The (Be + B)/C and (Z = 21–25)/Fe ratios are probably less influenced by a possible source component. We therefore utilize each of these measured ratios as a function of energy to deduce a point-by-point estimate of the material path length using the ratios calculated in 1 g cm^{-2} increments as a function of energy. This material path length is shown in Figure 16. Note that the path length deduced from the (Z = 21–25)/Fe ratio is generally slightly longer than that deduced from the (Be + B)/C ratio. This might suggest a small source component of one or more of the Z = 21–25 nuclei. Or it could be a measure of systematic effects in the propagation calculations. For example, a modified exponential path-length distribution, in which short path lengths are suppressed relative to long ones, can produce effects of this nature (e.g., Shapiro and Silberberg 1975; Simon 1977).

In order to bring the measured N/O and (F + Na + Al)/(Ne + Mg + Si) ratios into agreement with predictions based on Be + B and the Z = 21–25 nuclei, we must assume significant source components of N and (F + Na + Al). If we take $N_s = 0.065 O_s$ and (F + Na + Al)$_s$ = 0.065 (Ne + Mg + Si)$_s$, then the measured ratios give the apparent path lengths as a function of energy as indicated in Figure 16. These values are quite consistent with those determined from the (Be + B)/C and (Z = 21–25)/Fe ratios. Overall this is a very sensitive method of estimating the source composition of these nuclei—much more sensitive, for example, than utilizing a single measurement at a single energy as has been done in the past (e.g., Shapiro and Silberberg 1975).

The data from all secondary components give, we believe, a self-consistent value for the path length and

its variation with energy. The best-fit relationship between these quantities derived from all the data but weighting the (Be + B)/C ratio most heavily is

$$X = (7.2 \pm 1.2)E^{-0.30 \pm 0.06}, \qquad (10)$$

where X is in grams cm^{-2}, E in GeV per nucleon, in the range 1–50 GeV per nucleon. The specific energy dependence of this path length is of particular interest. Owens (1976) has discussed the dependence of the escape of cosmic rays on the diffusion coefficient in various propagation models, including the leaky-box model. He has pointed out several lines of evidence which suggest a diffusion coefficient $K \sim E^{0.3-0.5}$, which would lead to a path-length variation $X \sim E^{(-0.3-0.5)}$, and points out that a Kolmogorov spectrum of scattering irregularities incorporated in a simple model of interstellar diffusion, similar to that believed applicable in interplanetary space, leads to a value of $K \sim E^{0.33}$ or $X_e \sim E^{-0.33}$ very close to that we observe (strictly speaking, $K \sim P^{0.3-0.5}$ [P is the rigidity], which is $\sim E^{0.3-0.5}$ only at high energies).

Some observations of the path-length variation with energy give a stronger dependence than we observe. For example, Juliusson et al. (1975) quote $X_e \sim \epsilon^{-0.49 \pm 0.05}$, and Caldwell (1977) obtains $X_e \sim \epsilon^{-0.59 \pm 0.09}$, although some studies employing a larger body of early data have suggested less of an energy dependence (Cesarsky and Audouze 1974; Fontes 1977). Our own data suggest a milder path-length variation with energy than either of the Chicago experiments. It could be that the dependence of path length on energy increases with increasing energy. If this is the case, then our average exponent of 0.30 would be expected to be less than those derived by Juliusson et al. (1975) or Caldwell (1977), since the energy range covered by our experiment extends to lower energies than that covered by the above authors. The uncertainties in the data do not at present warrant a more detailed analysis of this point, although we

shall treat the situation below 1 GeV per nucleon separately later in this paper.

b) Primary-to-Primary Nucleus Ratios

It is natural to apply the results just obtained on the path-length dependence of cosmic-ray propagation to the ratios of various primary nuclei. Neglecting energy changes and the effects of fragmentation, the intensity of a primary nucleus in the leaky-box

$$j_i(E) = \frac{q_i(E)}{X_i^{-1} + [X_e(E)]^{-1}} , \qquad (11)$$

where $q_i(E)$ is the cosmic-ray source term and X_i and X_e are the interaction mean free path and the escape length, respectively. The ratio of the intensity of a lower Z primary (species i) to a higher Z primary (species k) is then given by

$$R \equiv \frac{j_i(E)}{j_k(E)} = \frac{X_k^{-1} + [X_e(E)]^{-1}}{X_i^{-1} + [X_e(E)]^{-1}} \frac{q_i(E)}{q_k(E)} , \qquad (12)$$

where $X_i > X_k$. If $q_i(E)/q_k(E)$ equals a constant S_i/S_k independent of energy (equal to the source ratio of these species) and if $X_e(E)$ decreases as E increases, then R also decreases as E increases, approaching the source ratio S_i/S_k at very large energies. The same behavior is observed for a solution of the full transport equation. The further the separation in Z of the primary nuclei, the greater the difference in the value of the interaction mean free path of these nuclei, and the larger the effect. In Figures 14 and 15 we show the predicted ratios for several combinations of primary nuclei. In these calculations, which use the full transport equation, we have taken all primary nuclei to have the same source spectrum energy dependence and have adjusted the source ratios to give a best fit to the observations. For all ratios covering a wide range of primary nuclei, the agreement between predictions and measurements is excellent over the energy range 1 to ~40 GeV per nucleon. We see no need to assume different source spectra for any of the primary nuclei over this energy range. This finding is made possible by the somewhat milder variations of the ratios with energy that we observe—particularly the (C + O)/Fe ratio—than some earlier observations. Our result is in essential agreement with the recent data of Caldwell (1977) in this respect.

c) Source Spectra

Much attention is usually placed on the charge ratios, and the actual details of the individual charge spectra of the primary nuclei are frequently overlooked. Interesting information is contained in the spectral exponents and their changes with energy. The governing equation for this behavior in the leaky-box model is equation (11). From this equation it is seen that at energies such that $X_e \ll X_i$ the kinetic energy spectral exponent observed at Earth will be steeper than that of the source spectrum by a factor $E^{-\alpha}$, where α specifies the energy dependence of the escape

length. If we take $\alpha = 0.3$, then the high-energy spectra of all nuclei should have an exponent 0.3 larger than the source spectra. For He this high-energy limit is applicable over the entire energy range greater than 1 GeV per nucleon; for C + O this limit is approached above 10 GeV per nucleon, whereas for Fe the limit is not approached until several hundred GeV per nucleon. Thus over the energy range we measure, the Fe spectral index is close to that of the source spectrum and is ~0.1–0.2 units flatter than the C + O spectrum and 0.3 units flatter than the He spectrum.

The He spectrum is essentially unaffected by the escape length variations, yet its kinetic energy spectral index is known to vary in a systematic way with energy (Webber and Lezniak 1974; Ramaty, Balasubrahmanyan, and Ormes 1973). For example, between 10 and 100 GeV per nucleon the best value of the spectral index for He is 2.64, whereas >100 GeV per nucleon the index steepens to 2.75 (Ramaty, Balasubrahmanyan, and Ormes 1973). Below 10 GeV per nucleon the index continues to flatten even at energies above where the solar modulation effects can be significant (Webber and Lezniak 1974). (See also Fig. 10.) This effect is unlikely to be related to a changing escape length with energy, but it could be an intrinsic property of the source spectrum itself (steepened by a power of 0.3 due to the changing escape length). If so, this behavior might also be apparent in the spectra of C + O and Fe nuclei. If one "corrects" the C + O spectrum for escape length variations relative to He, then indeed this (source) spectrum shows essentially the same changing exponent with energy as does He (see Fig. 10). The Fe spectrum is not determined over a wide enough energy range to verify that, when it is corrected for escape length variations, it too exhibits a changing exponent with energy. However, the possibility of a changing source spectral index with energy introduces complications in the interpretation of the data for all of the primary nuclei. Using the He spectrum as a guide, it appears that the cosmic-ray source spectrum changes slowly from a kinetic energy exponent ~2.25 − 0.30 = 1.95 at an energy ~5 GeV per nucleon to an exponent ~2.75 − 0.30 = 2.45 above 100 GeV per nucleon. On this picture it is easy to see why many measurements of the Fe spectrum have given exponents ~2.0–2.2 (e.g., Balasubrahmanyan and Ormes 1973); this would be the source spectrum at the relatively low energies at which the Fe spectral measurements have been made. To adequately understand these possible source spectral variations with energy and to separate out source effects from leaky-box model propagation effects requires the measurement of the Fe spectrum along with the lighter nuclei at energies well above 100 GeV per nucleon.

d) Charge Composition

It is evident from Figure 5 that the charge resolution is adequate to resolve adjacent charges, except for nuclei such as P and Mn which lie near much more abundant even nuclei. It is also evident from Table 3 that the statistical accuracy is sufficient to study the

spectra of individual charges. Our success in determining the source abundances for the more abundant secondary and primary nuclei by examining the charge ratios over a wide band of energies, as in Figures 12–15, suggests that we apply this procedure to the less abundant nuclei as well. We have therefore constructed graphs such as those in Figures 12–13 for all nuclei and compared the observations with the predictions for an energy-dependent escape length $\sim E^{-0.3}$. From these curves we have deduced the source abundance that best fits the data. These source abundances are shown in Table 6, normalized to the abundance of O = 1000. We also show in this table the normalized measured integral abundances above three energies. This illustrates a trend of the abundance ratios that asymptotically approaches the source abundance ratios at high energy. Also shown in this table are the most recent source abundances derived by Shapiro, Silberberg, and Tsao (1975) based mainly on data at one energy, ~ 1.5 GeV per nucleon.

There are several relatively mild differences between our source abundance ratios and those derived by Shapiro et al. These include (1) a source abundance of Na that is lower and is now consistent with zero; (2) a source abundance of Si that is somewhat higher; (3) an upper limit to the source abundance of both $Z = 17$–19 and $Z = 21$–25 nuclei. We have examined each charge in these groups individually and find all of them, with the possible exception of argon, consistent with a zero source abundance; however, we believe that upper limits on the entire groups of charges represent a more conservative interpretation

of the data. Of all of these charges, Shapiro, Silberberg, and Tsao 1975 find that only argon appears to have a significant source component. Our limits for the source abundances of the different charge groups are consistent with those of Shapiro et al., although our upper limit for the $Z = 21$–25 nuclei is higher than that obtained from their work. (4) Our source abundance of Ca ($Ca_s = 0.06$ Fe_s) is somewhat lower than that of Shapiro et al. and other earlier determinations. Larger fragmentation cross sections to Ca would further reduce this source abundance. This observation is consistent with the results of Simpson et al. 1977, who find that ^{40}Ca comprises $\leqslant 20\%$ of all Ca observed at Earth. (5) Our Fe abundance is significantly higher than earlier determinations. As near as we can determine, this is a result of our use of Fe nuclei data over a wide range of energies in our fit, along with an energy-dependent escape length.

e) Charge Ratios below 1 GeV per Nucleon

We treat the observations below 1 GeV per nucleon separately because of the fact that interplanetary energy loss effects may be important in this region. In Figures 12–15 we include the most recent data from the University of Chicago group at low energies (Garcia Munoz, Mason, and Simpson 1977a, b; Garcia Munoz et al. 1977), which we believe may be reliably compared with our own data at somewhat higher energies. For all secondary-to-primary ratios our data show a peak just below 1 GeV per nucleon and a falloff in the ratio at lower energies. Where

TABLE 6
COSMIC-RAY COMPOSITION

Charge	> 450 MeV/nuc	> 3 GeV/nuc	> 10.5 GeV/nuc*	Source	Shapiro et al. (1975)
He	44700 ± 500	41700 ± 800	...	26500 ± 500	23300
Li	192 ± 4	180 ± 8	...	~0	~0
Be	94 ± 2.5	87 ± 4	78 ± 8	~0	~0
B	329 ± 5	298 ± 9	201 ± 14	~0	~0
C	1130 ± 12	1077 ± 14	1030 ± 31	890 ± 20	901
N	278 ± 5	248 ± 9	188 ± 15	70 ± 10	72
O	1000	1000	1000	1000	1000
F	24 ± 1.5	16 ± 2	16 ± 6	< 4	0
Ne	158 ± 3	157 ± 6	147 ± 10	143 ± 8	135
Na	29 ± 1.5	22 ± 2	22 ± 7	6 ± 5	8
Mg	203 ± 3	201 ± 6	200 ± 12	210 ± 10	216
Al	36 ± 1.5	30 ± 3	34 ± 5	27 ± 8	21
Si	141 ± 3	153 ± 6	168 ± 12	206 ± 12	190
P	7.5 ± 0.6	7.0 ± 1.0	< 4	~0	≲2.2
S	34 ± 1.5	32 ± 2.2	34 ± 4	33 ± 3	27
Cl	9.0 ± 0.6	5.1 ± 0.9			≲.1
A	14.2 ± 0.9	10.1 ± 1.3	19 ± 4	< 7	6.5
K	10.1 ± 0.7	8.5 ± 1.2			≲1.1
Ca	26 ± 1.3	18 ± 1.9	15 ± 3.5	14 ± 3	21
Sc	6.3 ± 0.6	5.1 ± 0.9			0
Ti	14.4 ± 0.9	10 ± 1.3			≲1.1
V	9.5 ± 0.7	7.7 ± 1.1	36 ± 5	< 14	~0
Cr	15.1 ± 0.9	10.9 ± 1.4			≲3.0
Mn	11.6 ± 1.0	7.8 ± 1.3			≲1.1
Fe	103 ± 2.5	112 ± 5	157 ± 13	236 ± 16	198
Ni	5.6 ± 0.6	3.7 ± 0.9	4 ± 2	10 ± 1.5	7.5

* Average of data from 1974 and 1976 flights.

available, the Chicago data show a continuation of this trend. For the primary-to-primary ratios the Chicago data show a general continuation of the trend of our data at higher energies—with the exception of the C/Si ratio. The behavior of these primary-to-primary ratios at low energies is dependent on several factors. If the energy-dependent escape observed at higher energies continues below 1 GeV per nucleon, then these ratios should continue to increase although somewhat more slowly (Figs. 14a and 15a). If the escape length is constant below 1 GeV per nucleon, then the ratios should flatten appreciably (Figs. 14b and 15b). Interplanetary energy loss effects decrease the energy of interstellar particles ~ 100–200 MeV per nucleon at the time in the solar cycle at which these measurements are made. This has a relatively minor effect on the ratios above ~ 400 MeV per nucleon, becoming progressively larger at lower energies and causing the ratios to become even flatter. At energies ~ 200 MeV per nucleon all ratios should become flat as a result of this energy loss, no matter what the interstellar ratio.

The data are somewhat inconclusive and contradictory regarding the behavior of the path length below 1 GeV per nucleon. The C/Si, C/O, and $(C + O)/(Ne + Mg + Si)$ ratios are all more consistent with a constant escape length below 1 GeV per nucleon, with the possible effects of interplanetary energy loss being evident as well at the lowest energies. Our Si/Fe ratio is also consistent with this interpretation; however, the low-energy Chicago ratio is consistent with a continuing increase of escape length below 1 GeV/nuc. Earlier data from this group (Garcia Munoz et al. 1975), which gave an Si/Fe ratio in the range 1.5–1.6 at these energies, is more consistent with a constant escape length below 1 GeV per nucleon. And finally the C + O/Fe ratio is more consistent with an energy-dependent escape length below 1 GeV per nucleon when the low-energy Chicago data point is included.

The behavior of the secondary-to-primary ratios also can be interpreted directly in terms of the variation of escape length with energy through the use of the curves in Figure 16. As in the case of the primary-to-primary ratios, interplanetary energy loss effects should be relatively small above ~ 400 MeV per nucleon. The most accurately known of the secondary-to-primary ratios, the (Be + B)/C ratio, indicates very little if any escape-length variation below 1 GeV per nucleon. The other secondary-to-primary ratios are consistent with the behavior, although there are differences in the magnitude of the escape length, as noted earlier.

The behavior of the (Be + B)/C and $(Z = 21$–$25)/$Fe ratios at the lowest energies is puzzling when our data and the Chicago data on these nuclei are combined.

These ratios continue their decrease with energy below 1 GeV per nucleon, as noted in our higher-energy data, but this decrease is so large that it would appear that the escape length actually *decreases* at lower energies. Interplanetary energy loss effects will flatten these ratios, with the result that the decrease in the ratios below 1 GeV per nucleon at Earth will be less than that calculated for interstellar space. The observations will thus imply an even greater decrease in escape length (e.g., from 7.2 g cm^{-2} at 1 GeV per nucleon to $\leqslant 6$ g cm^{-2} at 100 MeV per nucleon) if interplanetary energy loss effects are important.

X. SUMMARY

We have measured the energy spectra and charge ratios of cosmic-ray nuclei in the energy range from ~ 300 MeV per nucleon to 50 GeV per nucleon. When comparing the ratio of secondary nuclei to primary nuclei, we find that the data are consistent with an escape-length variation $X = (7.2 \pm 1.2)E^{-0.30 \pm 0.06}$ g cm^{-2} above ~ 1 GeV per nucleon. This energy dependence can be reconciled with a Kolmogorov spectrum of interstellar scattering irregularities in a simple resonant-scattering model for cosmic-ray diffusion in the Galaxy. The primary-to-primary nucleus ratio changes we observe are consistent with this escape-length variation and do not require the assumption of different source spectra for different nuclei.

We point out that, because of the escape-length variation with energy, the exponent of the source spectrum of cosmic rays must be 0.3 smaller than the high-energy spectra observed at Earth. From an examination of the He spectrum it is concluded that the exponent of the kinetic energy source spectrum is not constant with energy but increases slowly from ~ 1.95 at an energy ~ 5 GeV per nucleon to 2.45 above 100 GeV per nucleon.

Utilizing the individual charge ratios measured over a broad band of energies, we have determined a new set of cosmic-ray source abundances. The abundances of N, Na, Si, Ca, and Fe differ from earlier determinations.

The behavior of the charge ratios below 1 GeV per nucleon is examined, and it is found that the data are most consistent with an energy-independent escape length at these lower energies. Several anomalies to this picture exist in the low-energy data, however, the most obvious being the relatively large decrease in the (Be + B)/C ratio. This suggests that the escape length actually decreases at lower energies and/or interplanetary energy loss effects are less important than usually assumed.

REFERENCES

Balasubrahmanyan, V. K., and Ormes, J. F. 1973, *Ap. J.*, **186**, 109.
Caldwell, J. H. 1977, *Ap. J.*, **218**, 269.
Cesarsky, C. S., and Audouze, J. 1974, *Astr. Ap.*, **30**, 119.
Cowsik, R., Pal, Yash, Tandon, S. N., and Verma, R. P. 1965, *Phys. Rev.*, **158**, 1238.

Fontes, P. 1977, *Phys. Rev. C.*, **15**, 2159.
Garcia Munoz, M., Juliusson, E., Mason, G. M., Meyer, P., and Simpson, J. A. 1975, *Ap. J.*, **197**, 489.
Garcia Munoz, M., Mason, G. M., and Simpson, J. A. 1977a, *Proc. 15th International Cosmic Ray Conf.*, Plovdiv, Paper OG-61.
———. 1977b, *Proc. 15th International Cosmic Ray Conf.*, Plovdiv, Paper OG-84.
Garcia Munoz, M., Mason, G. M., Simpson, J. A., and Wefel, J. P. 1977, *Proc. 15th International Cosmic Ray Conf.*, Plovdiv, Paper OG-62.
Juliusson, E. 1974, *Ap. J.*, **191**, 331.
Juliusson, E., Cesarsky, C. J., Meneguzzi, M., and Casse, M. 1975, *Proc. 14th International Cosmic Ray Conf.*, Munich, **2**, 653.
Juliusson, E., Meyer, P., and Müller, D. 1972, *Phys. Rev. Letters*, **29**, 445.
Lezniak, J. A. 1975, *Nucl. Instr. Meth.*, **126**, 129.
———. 1976, *Nucl. Instr. Meth.*, **136**, 299.
———. 1977, unpublished.
Lindstrom, P. J., Greiner, D. E., Heckman, H. H., Cork, B., and Bieser, F. S. 1975, preprint LBL No. 3650.
Lund, N. 1975, *Proc. 14th International Cosmic Ray Conf.*, Munich, **11**, 3746.
Maehl, R. C., Ormes, J. F., Fisher, A. J., and Hagen, F. A. 1976, *Ap. Space Sci.*, **47**, 163.

Ormes, J. F., and Balasubrahmanyan, V. K. 1973, *Nature*, **241**, 95.
Owens, A. J. 1977, *Ap. Space Sci.*, **44**, 35.
Ramaty, R., Balasubrahmanyan, V. K., and Ormes, J. F. 1973, *Science*, **180**, 731.
Shapiro, M. M., and Silberberg, R. 1975, *Phil. Trans. Royal Soc. London*, A**277**, 317.
Shapiro, M. M., Silberberg, R., and Tsao, C. H. 1975, *Proc. 14th International Cosmic Ray Conf.*, Munich, **2**, 532.
Simon, M. 1977, *Proc. 15th International Cosmic Ray Conf.*, Plovdiv, **1**, 125.
Simpson, G. A. 1977, Ph.D. thesis, University of New Hampshire.
Simpson, G. A., Kish, J., Lezniak, J. A., and Webber, W. R. 1977, *Ap. Letters*, **19**, 3.
Smith, L. H., Buffington, A., Smoot, G. F., and Alvarez, L. W. 1973, *Ap. J.*, **180**, 987.
Webber, W. R., Damle, S. V., and Kish, J. C. 1972, *Ap. Space Sci.*, **15**, 245.
Webber, W. R., and Lezniak, J. A. 1974, *Ap. Space Sci.*, **30**, 361.
Webber, W. R., Lezniak, J. A., and Kish, J. C. 1973, *Nucl. Instr. Meth.*, **111**, 301.
Webber, W. R., Lezniak, J. A., Kish, J. C., and Damle, S. V. 1973, *Nature*, **241**, 96.

J. A. LEZNIAK and W. R. WEBBER: Physics Department, Space Science Center, DeMeritt Hall, University of New Hampshire, Durham, NH 03824